Adjusting solar-induced fluorescence to nadir-viewing provides a better proxy for GPP

Dalei Hao, Yelu Zeng, Zhaoying Zhang, Yongguang Zhang, Han Qiu, Khelvi Biriukova, Marco Celesti, Micol Rossini, Peng Zhu, Ghassem R. Asrar, et al.

Adjusting Solar-induced Fluorescence to Nadir-viewing Provides a Better Proxy for GPP

Dalei Hao[1], Yelu Zeng[1,7,*], Zhaoying Zhang[2], Yongguang Zhang[2,3], Han Qiu[1,7], Khelvi Biriukova[4], Marco Celesti[4], Micol Rossini[4], Peng Zhu[5], Ghassem R. Asrar[6], and Min Chen[1,7,8,*]

[1]Joint Global Change Research Institute, Pacific Northwest National Laboratory, College Park, MD, USA.

[2]International Institute for Earth System Sciences, Nanjing University, Nanjing, China.

[3]Jiangsu Provincial Key Laboratory of Geographic Information Science and Technology, Key Laboratory for Land Satellite Remote Sensing Applications of Ministry of Natural Resources, School of Geography and Ocean Science, Nanjing University, Nanjing, Jiangsu, China.

[4]Remote Sensing of Environmental Dynamics Laboratory, Department of Earth and Environmental Sciences (DISAT), University of Milano-Bicocca, Piazza della Scienza 1, Milano, Italy.

[5]Laboratoire des Sciences du Climat et de l'Environnement, CEA-CNRS-UVSQ, UMR8212, Gif-sur-Yvette, France.

[6]Universities Space Research Association, Columbia, MD, USA.

[7]Department of Forest and Wildlife Ecology, University of Wisconsin-Madison, Madison, WI, USA

[8]Nelson Institute Center for Climatic Research, University of Wisconsin-Madison, Madison, WI, USA

Corresponding author: Min Chen (mchen392@wisc.edu); Yelu Zeng (zeng74@wisc.edu)

Abstract

Solar-induced fluorescence (*SIF*) provides key information for inferring terrestrial gross primary productivity (*GPP*). However, there is little research on analyzing the performance of nadir-adjusted *SIF* (SIF_{nadir}) on *GPP*, compared to total *SIF* emitted by all leaves (SIF_{total}) for reducing the viewing angle effects and estimating *GPP*. Besides, there have been controversial opinions on whether SIF_{total} is better correlated to *GPP* than raw SIF observations (SIF_{obs}). Here we systematically analyzed the relationship between raw/nadir/total *SIF* (i.e., SIF_{obs}, SIF_{nadir} and SIF_{total}) and *GPP* and investigated the underlying mechanism, using multi-angular field measurements and eddy covariance data in wheat and corn crops at sub-daily scale. We further compared the performance of SIF_{obs}, SIF_{nadir} and SIF_{total} in estimating GPP using the TROPOspheric Monitoring Instrument (TROPOMI) *SIF* and concurrent AmeriFlux measurements at daily scale. The results indicate that diurnal SIF_{nadir} has stronger correlations to *GPP* than SIF_{obs} for field measurements, with the increase of mean coefficient of determination (R^2) by 0.05~0.07 for far-red band and 0.11~0.20 for red band. SIF_{nadir} shows comparable performance with SIF_{total} for both far-red and red bands. Although the viewing angle effects dominate the difference in estimating GPP between SIF_{nadir} and SIF_{obs}, the correlation between light use efficiency (*LUE*) and f_{esc} further determines the different performance of SIF_{nadir} and SIF_{total} in estimating GPP. TROPOMI-based analysis further confirms that SIF_{nadir} overall has higher correlations to AmeriFlux *GPP* than SIF_{obs} for different plant functional types and shows similar performance with SIF_{total}. Compared to SIF_{total}, the estimation of SIF_{nadir} independent of viewing angle effects does not require any canopy structure parameters, and thus offers promising potential for reliably estimating regional and global *GPP*.

Keywords: SIF, gross primary productivity, viewing-angle effects, nadir viewing, canopy structure effects, TROPOMI.

1 Introduction

The emerging spaceborne solar-induced fluorescence (*SIF*) measurements offer a novel opportunity for monitoring and interpreting large-scale ecosystem carbon cycle (Frankenberg et al., 2011; Joiner et al., 2011; Magney et al., 2020; Meroni et al., 2009; Mohammed et al., 2019; Ryu et al., 2019). Compared to traditional vegetation indices, *SIF* has more inherent linkages to vegetation photosynthetic activities (Gu et al., 2019; Magney et al., 2019). *SIF* has been increasingly used for tracking terrestrial gross primary productivity (*GPP*) (Sun et al., 2017), detecting plant stress (He et al., 2020b; Song et al., 2018), monitoring vegetation phenology (Wang et al., 2019; Zhang et al., 2020a), estimating crop yield (Guan et al., 2016; He et al., 2020a) and diagnosing ecosystem transpiration (Lu et al., 2018; Maes et al., 2020; Shan et al., 2019; Shan et al., 2021).

However, viewing-angle effects have considerable impact on the top-of-canopy *SIF* observations (SIF_{obs}) and their applications. Similar to surface reflectance, SIF_{obs} is sensitive to viewing angles due to the canopy scattering and re-absorption processes (Van der Tol et al., 2019), which has been confirmed by field measurements (Biriukova et al., 2020; Liu et al., 2015; Pinto et al., 2017; Rogers et al., 2020; Zhang et al., 2020c), model simulations (Sakai et al., 2020; Zeng et al., 2020; Zhao et al., 2016) and remote sensing observations (Doughty et al., 2019; Guanter et al., 2012). The viewing-angle effects on *SIF* can distort the *SIF-GPP* relationship (Zhang et al., 2019a; Zhang et al., 2018b; Zhang et al., 2021). Considering that most existing and upcoming *SIF* observations from spaceborne instruments such as the Second Global Ozone Monitoring Experiment (GOME-2), Orbiting Carbon Observatory-2 (OCO-2) and TROPOspheric Monitoring Instrument (TROPOMI) have varying scanning angles, reducing the view-angle effects is urgently needed for *SIF* applications.

Compared to SIF_{obs}, the total *SIF* emitted by all leaves (hereinafter referred to as total *SIF,* SIF_{total}) is less affected by scattering and reabsorption processes, and thus has been considered to be better correlated to *GPP* (He et al., 2017; Lu et al., 2020; Zhang et al., 2019b; Zhang et al., 2020b; Zhang et al., 2020c). A few recent studies developed practical methods to estimate SIF_{total} based on radiative transfer modeling (Liu et al., 2019; Yang and Van der Tol, 2018; Yang et al., 2020; Zeng et al., 2019). These methods typically require knowledge of canopy structure parameters such as leaf area index (*LAI*), clumping index (*CI*) and leaf angle distribution (*LAD*), but their estimations from remote sensing still have large uncertainties (Fang et al., 2019; Pisek et al., 2015; Zhang et al., 2020d) and hinder robust applications of SIF_{total}.

Moreover, there have been controversial opinions on whether SIF_{total} is better correlated to *GPP* than SIF_{obs}. Zhang et al. (2019, 2020b) used the spaceborne TROPOMI and OCO-2 data and demonstrated that SIF_{total} outperformed SIF_{obs} because of the reduced impact of canopy structure effect. Lu et al. (2020) showed SIF_{total} improved the estimate of diurnal *GPP* at Harvard Forest with complex canopy structure. Zhang et al. (2020c) showed that SIF_{total} had less angular dependencies and stronger relationship with GPP in crops. In contrast, Dechant et al. (2020) showed SIF_{obs} better served as a proxy for *GPP* in crops, benefited by the positive correlations of the ratio of *SIF* photons escaping from canopy with photosynthetic light use efficiency (*LUE*). It is worth noting that the viewing angle of *SIF* measurements was fixed at nadir or hemispheric in Dechant et al. (2020), whereas *SIF* observations were collected at varying viewing angles in Zhang et al. (2019, 2020b, 2020c), and with a fixed view zenith angle (*VZA*) of 30° in Lu et al. (2020). The datasets used in the existing studies were collected using different modes of fixed (nadir or off-nadir) or varying viewing angles, and thus the conclusions of these studies may not be directly comparable and scalable. The viewing-angle effects have

105 smaller impacts on analyzing the *SIF-GPP* relationship in Dechant et al. (2020) due to nadir or
106 hemispherical viewing conditions, as compared with other studies (e.g., Zhang et al. (2019,
107 2020b, 2020c) and Lu et al. (2020)) with time varying viewing conditions, which may explain
108 the contradictory conclusions from these studies.

109 Therefore, normalizing SIF_{obs} to a standard viewing angle (i.e., nadir in this study) is
110 proposed in this study to minimize the viewing-angle effects on SIF_{obs}. This effort will facilitate
111 a systematic analysis on the impacts of viewing angle on the *SIF-GPP* relationship and an
112 evaluation of the capabilities of nadir-adjusted *SIF* (SIF_{nadir}) and SIF_{total} for approximating GPP,
113 which can potentially resolve the aforementioned debate. To the best of our knowledge, no such
114 analysis has been carried out before. Compared to off-nadir viewing angles, SIF_{nadir} is less prone
115 to be affected by hotspot effects caused by the variation of solar angles (Hao et al., 2021a). Liu et
116 al. (2016) explored the potential of kernel-driven (KD) Bidirectional-Reflectance-Distribution-
117 Function (BRDF) models in fitting multi-angular *SIF* measurements. Hao et al. (2021b)
118 developed two practical methods to normalize *SIF* to nadir-viewing: one was based on multi-
119 angular reflectance while the other leveraged a KD model (Hao et al., 2020b). Neither method
120 requires input of canopy structural parameters, and their performance only depends on high-
121 quality reflectance and *SIF* data.

122 Our study aims to comprehensively assess and understand the performance of SIF_{nadir}
123 and SIF_{total} on approximating *GPP* estimations. We primarily focus on answering the following
124 four questions : 1) how effective are different *SIF* normalization methods in reducing the
125 viewing-angle effects? 2) how does SIF_{obs} normalized to nadir viewing perform in estimating
126 *GPP*, compared to the raw off-nadir SIF_{obs}? 3) which is better for estimating photosynthesis,

127 SIF_{nadir} or SIF_{total}? and 4) what are the contributing factors leading to the differences between
128 the performance of SIF_{nadir} and SIF_{total}?

129

130 **2 Materials and methods**

131 **2.1 Multi-angular field SIF measurements at sub-daily scale**

132 First, two field datasets (wheat and corn crops) were used in our analysis, with the
133 characteristics presented in Table 1. Both wheat and corn canopies show the erectophile leaf
134 inclination distribution (empirically identified from the field). Specifically, a high-resolution
135 spectrometer QEPro (Ocean Optics, Dunedin, FL, USA) installed in a multi-angular
136 measurement system (Multi-Fluo) was used to collect multi-angular observations. It had a field-
137 of-view (FOV) of 25° and a spectral range of 650-800 nm, with a full width at half maximum of
138 0.3 nm. For each day, the Multi-Fluo system (Figure S1) collected 24 groups (with different
139 VZAs) of multi-angular data from 6:00 to 18:00 (UTC+8). The system acquired one group of
140 multi-angular observations with the same VZA every 30 min, which covered 25 different view
141 azimuth angles (*VAA*) changing from 60° to 300° at a 10° interval. During the measurements,
142 *VZA* was dynamically adjusted to track the solar zenith angle (*SZA*) and to capture the hotspot
143 effects, and it was fixed at 40° when *SZA*>40° to avoid the effects of large instantaneous FOVs.
144 An advanced spectral fitting method (Cogliati et al., 2015) was used to retrieve *SIF* for far-red
145 (760 nm) and red (687 nm) wavelengths. We used the averaged reflectance for 686-691 nm and
146 757-768 nm spectral bandwidths as Red and near-infrared (NIR) reflectance, respectively.
147 During the growing season, an eddy covariance flux system was installed to continuously
148 measure net ecosystem CO_2 exchange (*NEE*). Accompanying meteorological data composed of

149 shortwave radiation, air temperature, relative humidity and vapor pressure deficit were observed
150 regularly. *GPP* was estimated at a half-hourly interval using a nighttime-based partitioning
151 method (Reichstein et al., 2005) provided in the REddyProc tool (Wutzler et al., 2018). Effective
152 *LAI* (equal to $LAI \cdot CI$, denoted as *eLAI*) was measured with LAI-2200 plant canopy analyzer (LI-
153 COR, Lincoln, NE, USA). The photosynthetically active radiation (*PAR*) and fraction of *PAR*
154 absorbed by chlorophyll (*FPAR*) were measured via six LI-190SL quantum sensors (LI-COR
155 Inc., Lincoln, NE, USA) installed both above and below the canopy, and *LUE* was calculated as
156 $GPP/(PAR \cdot FPAR)$. We only used the data acquired under clear sky conditions when the
157 clearness index (defined as the ratio of top-of-canopy to top-of-atmosphere solar radiation) was
158 larger than 0.6 to avoid the interference of clouds. Finally, the field data obtained for five days
159 were used in the analysis. Detailed descriptions of the field datasets and associated quality
160 control can be found in Zhang et al. (2020c).
161

Table 1. Characteristics of the field measurements for wheat and corn crops.

Variables		Wheat	Corn
Location	Latitude (°N)	34.5199	34.5199
	Longitude (°E)	115.5916	115.5916
Measured Time	Year	2018	2018
	Day of Year (DOY)	124-133	235-239
	Hour of day	6:00-18:00	6:00-18:00
Viewing angle	View Zenith Angle (*VZA*, °)	20-40	15-40
	View Azimuth Angle (*VAA*, °)	60-300 at 10 intervals	60-300 at 10 intervals
Leaf parameter	Leaf chlorophyll content (*Cab*, μg cm^{-2})	66-71	51-54
Canopy structure	Effective leaf area index (e*LAI*, m^2 m^{-2})	5.2-5.8	2.8-2.9
	Leaf inclination angle distribution	Erectophile	Erectophile
Field Image			

2.2 TROPOMI *SIF* and MODIS data

We also used daily TROPOMI *SIF* data over 2018-2019 together with corresponding MODIS products and flux tower GPP data from AmeriFlux sites (see Section 2.3) to evaluate our analysis at the large spatial scale. TROPOMI onboard the Sentinel-5 Precursor provides near-daily (around 13:30) *SIF* data with global coverage and a spatial resolution of 3.5-km × 7-km at nadir (Köhler et al., 2018). Considering that retrieved red *SIF* from TROPOMI still has high relative uncertainties (Köhler et al., 2020), we only used far-red (740 nm) *SIF* in this study. We used both instantaneous and daily averaged *SIF* and calculated the daily averaged *SIF* using the day-length correction factors (Zhang et al., 2018a). To reduce the cloud contamination and keep the most possible valid *SIF* data, the *SIF* soundings with the cloud fraction greater than 0.5 were excluded and the sensitivity of our results to this threshold was tested (see Section 3.3). Considering the large uncertainty in a single TROPOMI measurement (Köhler et al., 2018), *SIF* measurements centering within a 10-km radius of the flux towers were averaged to reduce the SIF uncertainties (Frankenberg et al., 2014) and match the AmeriFlux *GPP*.

A set of 500-m MODIS data were collected at the selected AmeriFlux sites using the Google Earth Engine (GEE) (Gorelick et al., 2017) to provide vegetation information. Specifically, the IGBP layer in the yearly MCD12Q1-v6 land cover products (Friedl et al., 2002) for 2018 was used to evaluate the homogeneity of AmeriFlux sites. The sites with larger than 50% being covered by the dominant PFT within a 10-km radius of the tower were considered as homogeneous. The 4-day MCD15A3H-v6 *LAI*/*FPAR* products (Myneni et al., 2002b) were selected to provide *LAI* and *FPAR*. The 8-day *CI* data retrieved from MODIS were acquired from Wei et al. (2019). Daily MCD43A1-v6 BRDF/Albedo Model Parameters products (Schaaf et al., 2002) were used to estimate multi-angular reflectance. The MODIS pixels within a 1.5-km

190 radius of the flux towers were spatially-averaged and temporally-interpolated using a nearest
191 neighbor methods to match with the AmeriFlux *GPP*.
192
193 **2.3 AmeriFlux *GPP* data**
194 Overall, 102 AmeriFlux sites which have coincident measurements with TROPOMI *SIF*
195 during 2018-2019 were selected for our analysis (see Table S1 and Figure 1 for site information
196 and spatial distribution, respectively). These sites cover eight International-Geosphere-
197 Biosphere-Programme (IGBP) PFTs (Belward et al., 1999): Evergreen needleleaf forests (ENF),
198 Deciduous broadleaf forests (DBF), Mixed forests (MF), Open shrublands (OSH), Woody
199 savannas (WSA), Grasslands (GRA), Wetlands (WET), and Croplands (CRO). Half-hourly *GPP*
200 data estimated from partitioning NEE measurements at these sites were aggregated to acquire the
201 daily values. Both half-hourly and daily *GPP* data were used to match with the instantaneous and
202 daily averaged TROPOMI *SIF* data, respectively. Only the *GPP* data during the growing seasons
203 from April to October were used to avoid the impact of dormancy in winter.
204
205

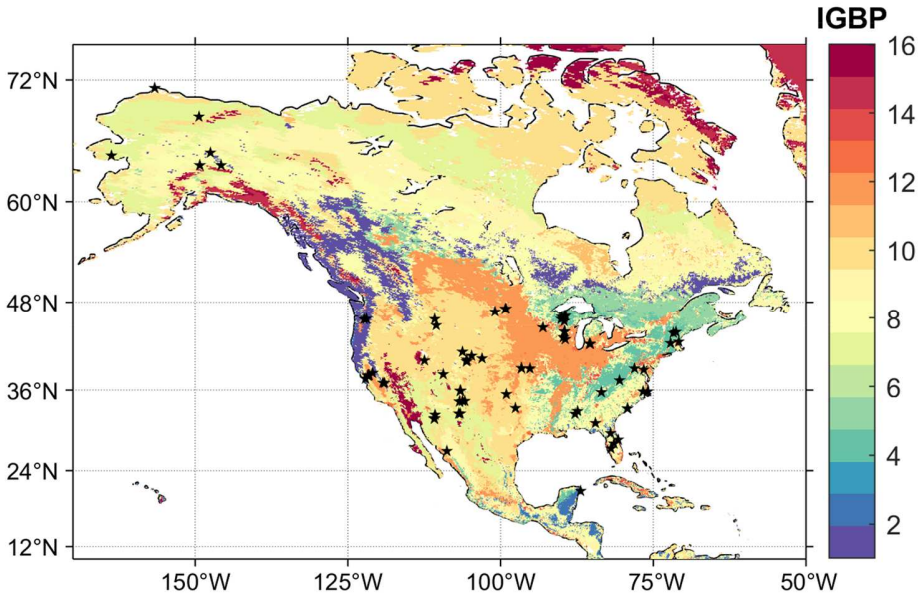

Figure 1. Spatial distribution of AmeriFlux sites used in our study. Black pentagram represents the site location. The background color represents the IGBP PFTs: 1: Evergreen needleleaf forests, ENF; 2: Evergreen broadleaf forests, EBF ; 3: Deciduous needleleaf forests, DNF; 4: Deciduous broadleaf forests, DBF; 5: Mixed forests, MF; 6: Closed shrublands, CSH; 7: Open shrublands, OSH; 8: Wood savannas, WSA; 9: Savannas, SAV; 10: Grasslands, GRA; 11: Permanent wetlands, WET; 12: Croplands, CRO; 13: Urban and built-up lands, URB; 14: Cropland/natural vegetation mosaics: CVM; 15: Snow and ice, SNO; and 16: Barren, BSV.

2.4 Decoupling viewing-angle and scattering/reabsorption effects on *SIF*

2.4.1 Overall framework

Due to the BRDF effect, SIF_{obs} is impacted by both the solar and viewing angles. With a certain solar angle, SIF_{obs} at a wavelength (λ) and a viewing angle (Ω) can be conceptually modeled as (Lee et al., 2013; Sun et al., 2017):

$$SIF_{obs}(\Omega,\lambda) = PAR \cdot FPAR \cdot \Phi_F(\lambda) \cdot f_{esc}(\Omega,\lambda) \quad (1)$$

where Φ_F is the quantum yield of *SIF*, and f_{esc} represents the fraction of *SIF* photons escaping from canopy. The product of first three terms represents SIF_{total} within a canopy.

We can directly derive SIF_{total} from SIF_{obs} using Equation 1 as:

$$SIF_{total}(\lambda) = \frac{SIF_{obs}(\Omega,\lambda)}{f_{esc}(\Omega,\lambda)} \quad (2)$$

Equation 2 suggests that the effects of viewing-angle and scattering/reabsorption can be simultaneously minimized. However, to evaluate their separate effects on SIF_{obs}, we need to decouple them into two independent terms. A practical solution for achieving this objective is to: 1) normalize SIF_{obs} with varying viewing angles to a standard viewing geometry (e.g., nadir) and 2) estimate SIF_{total} from SIF_{nadir}. In the first step, all *SIF* observations are corrected to an identical viewing angle and thus the viewing-angle effects are minimized/eliminated; and in the second step, the scattering/reabsorption effects can be further minimized by estimating SIF_{total}.

2.4.2 Calculating f_{esc} for deriving total *SIF*

Equation 2 shows that the key to disentangling the effects of viewing-angle and scattering/reabsorption is to accurately calculate f_{esc}. Based on the spectral invariants theory, Yang et al. (2018b) derived a simple method to calculate far-red f_{esc}:

$$f_{esc}(\Omega, far\_red) = \frac{Ref(\Omega,far\_red)}{i_0 \cdot \omega(far\_red)} \quad (3)$$

where Ref represents the NIR reflectance, i_0 is the canopy interceptance which represents the probability of a photon interacting with the vegetation canopy (Smolander and Stenberg, 2005), and ω is the leaf single scattering albedo (equal to the sum of leaf reflectance and transmittance). This method is only suitable for dense vegetation canopy (Yang et al., 2018b). Zhang et al. (2020c) used this equation to empirically estimate red f_{esc}. i_0 can be calculated using canopy structure parameters (Chen and Leblanc, 2001):

$$i_0 = 1 - \exp\left(\frac{-G(SZA)\cdot LAI\cdot CI}{\cos(SZA)}\right) \quad (4)$$

where $G(SZA)$ is the leaf projection function which quantifies the projection coefficient of unit foliage area on a plane perpendicular to the illumination direction. This method requires accurate canopy structure parameters (e.g., *LAI*, *CI* and *LAD*).

Meanwhile, Zeng et al. (2019) developed a practical method for estimating far-red f_{esc} using the near-infrared reflectance of vegetation ($NIRv$) (Badgley et al., 2017) and $FPAR$:

$$f_{esc}(\Omega, far\_red) = \frac{NIRv(\Omega)}{FPAR \cdot \omega(far\_red)} \quad (5)$$

$$NIRv \approx NIR \cdot NDVI \quad (6)$$

where $NIRv$ represents the fraction of reflected NIR light that originates from vegetation, and $NDVI$ is the normalized difference vegetation index (Tucker, 1979). This method requires accurate estimation of $NIRv$ and $FPAR$. Compared to Eq. 3, this method is suitable for both dense and sparse vegetation canopies (Zeng et al., 2019).

Similarly, Liu et al. (2020) developed a method for estimating red f_{esc} using the red reflectance of vegetation ($Redv$) and $FPAR$:

$$f_{esc}(\Omega, red) = \frac{Redv(\Omega)}{FPAR \cdot \omega(red)} \quad (7)$$

$$Redv(\Omega) \approx Red \cdot NDVI^2 \quad (8)$$

where $Redv$ represents the fraction of reflected red light that originates from vegetation. $NDVI^2$ is used to reduce the contribuition of soil to red reflectance, which is only an approximation acquired based on the PROSAIL model (Liu et al., 2020). This method also requires an accurate estimation of $Redv$ and $FPAR$.

Hereinafter, we named the methods expressed in Equations 3-4 and Equation 5-8 as i_0-based and $FPAR$-based methods, respectively. In this study, we also compared the difference between derived SIF_{total} using Ref (Equation 3) and $NIRv$ (Equation 6) or $Redv$ (Equation 8).

2.4.3 Viewing-angle normalization methods

Based on Equation 1, SIF_{nadir} can be calculated by

$$SIF_{nadir}(\lambda) = SIF_{obs}(\Omega,\lambda) \cdot \frac{f_{esc}(nadir,\lambda)}{f_{esc}(\Omega,\lambda)} \quad (9)$$

Combining Equations 5-8 and 9, we can normalize SIF_{obs} to SIF_{nadir} only with $NIRv$ or $Redv$ at both nadir and observed directions, which can be acquired from the KD model. This method is hereafter referred as the $NIRv/Redv$-based method. This method is applicable when multi-angular reflectance data are available, but its performance depends on the reduced sensitivty of *NIRv* and *Redv* to soil contribution (Hao et al., 2021b).

Hao et al. (2021b) suggested an alternative method that uses the KD model to fit *PAR*-normalized multi-angular *SIF* observations (hereinafter referred to as KD-based method):

$$\frac{SIF_{obs}(\Omega,\lambda)}{PAR} = f_{iso}(\lambda) \cdot K_{iso}(\Omega) + f_{vol}(\lambda) \cdot K_{vol}(\Omega) + f_{geo}(\lambda) \cdot K_{geo}(\Omega) \quad (10)$$

where f_{iso}, f_{vol} and f_{geo} represent the fitting parameters, and K_{iso}, K_{vol} and K_{geo} represent the isotropic, volumetric-scattering and geometric-optical kernels. In this study, we used a constant value of 1, RossThick kernel and LiTransit kernel as K_{iso}, K_{vol} and K_{geo}, respectively, to capture the BRDF shapes caused by volumetric-scattering and surface-scattering. The RossThick kernel was derived from a single scattering approximation of the radiative transfer theory for dense vegetation canopy (Roujean et al., 1992), and the LiTransit kernel was derived from the geometric-optical mutual shadowing BRDF model for sparse vegetation canopy (Li et al., 1999). RossThick kernel and LiTransit kernel can be used to characterize bowl-shaped and dome-shaped BRDF curves, respectively.

Considering relatively small variations of Φ_F within one day (Yang et al., 2018) or during the growing season (Wang et al., 2020) and relatively stable canopy structure in a short time period, we can use multiple *SIF* observations to fit the KD model in Equation 10 and then derive the ratio of SIF_{nadir} to SIF_{obs}. This method is efficient only when multi-angular *SIF* and *PAR* data are available, and its performance also depends on employed KD models (Hao et al., 2021b).

2.5 Analysis and evaluation methods

Using the field dataset at sub-daily scale, we first fitted the KD models to all reflectance and *SIF* observations for each day; then used the fitted models to calculate nadir reflectance and *SIF* at each time of that day. Finally, SIF_{nadir} and SIF_{total} were estimated using the methods in Sections 2.4.2 and 2.4.3. We evaluated the performance of adjusted *SIF*s by four methods (two methods for estimating SIF_{nadir} and two methods for estimating SIF_{total}) for estimating *GPP*. Note that for i_0-based and $FPAR$-based methods, ω were assumed as 0.9 and 0.1 for far-red and red bands, respectively (Liu et al., 2019), assuming that ω has little variation during the short measurement periods (Table 1). i_0 was estimated based on measured *eLAI* and a simplified approximation of $G(SZA)$=0.5 under the spherical distribution. For the $FPAR$-based method, we used the measured *FPAR*. We assume that the *SIF* variation is caused mainly by the variation of viewing angle in a short time window (i.e., 30 min) under no-stress conditions and thus the coefficient of variation (CV) was used to evaluate the performance of different methods for reducing the viewing-angle effects, calculated as the ratio of standard deviation to mean value:

$$CV = \frac{std(\{SIF_i\})}{mean(\{SIF_i\})} \quad (11)$$

$where$ $\{SIF_i\}$ represents the group of observed/nadir/total *SIF*. Specifically, we calculated the CVs for each group of *SIF* values with the same *VZA* but different *VAA*s, where the raw *SIF*

observed data were acquired at a short time window of about 30 min and thus the variation of the solar angle can be neglected. Smaller CVs indicate better performance for reducing the viewing-angle effects.

We used both linear and hyperbolic models (Damm et al., 2015) to approximate the empirical *SIF-GPP* relationship:

$$GPP = a1 \cdot SIF + b1 \quad (12)$$

$$GPP = \frac{a2 \cdot SIF}{SIF + b2} \quad (13)$$

where SIF represents observed/nadir/total *SIF*, and $a1$, $a2$, $b1$ and $b2$ are the fitting parameters. We used the coefficient of determination (R^2) and root mean square errors (RMSE) to test the goodness of fit for linear models, and the RMSE for hyperbolic models. The relationship was considered statistically significant if the significance level (p-value) was smaller than 0.05.

We used the TROPOMI and AmeriFlux data (both instantaneous at the overpass time of TROPOMI and daily averaged values) over the 2018-2019 period to evaluate the *SIF-GPP* relationship at the large spatial scale. Table S2 provides an overview of the data source for canopy structure parameters and reflectance, used for different methods. With the KD-based method, TROPOMI SIF data in a 16-day window were used to fit the parameters in the KD model. With the i_0-based method, the far-red ω were assumed to be 0.9 (Asner, 1998; Gates et al., 1965; Liu et al., 2019) and relatively conservative both within and across species and is relatively invariant across time and space. LAD was assumed to be spherical, and then i_0 was estimated using MODIS LAI and CI data. With the $FPAR$-based method, ω was also assumed to be 0.9 and MODIS $FPAR$ data was used. The magnitude of far-red ω only affected the magnitude of f_{esc} and had minimal impacts on the results in our study due to its small variations with time.

334

335 **3 Results**

336 **3.1 Minimizing viewing-angle effects on *SIF***

337 Both SIF_{nadir} and SIF_{total} reduce the angular heterogeneity of *SIF* observations in wheat
338 and corn, compared to raw directional *SIF* observations (Figures 2 and 3). Overall, the KD model
339 fits well with the reflectance and *SIF* for wheat and corn (Figure 2). Nadir *SIF* has smaller CVs
340 than the raw directional *SIF* observations (Figure 3). For wheat, nadir *SIF* normalized by
341 $NIRv/Redv$-based method has mean CVs of about 14.2% (far-red) and 29.8% (red), and the
342 mean CVs of KD-based method are 17.7% (far-red) and 25.3% (red), while the raw multi-
343 angular observations have mean CVs of 18.7% (far-red) and 44.6% (red). For corn, nadir *SIF*
344 normalized by $NIRv/Redv$-based method has mean CVs of 14.0% (far-red) and 24.7% (red), and
345 the mean CVs of KD-based method are 18.7% (far-red) and 22.8% (red), while observed *SIF* has
346 CV values of 20.5% and 32.8%, respectively. In contrast, the two methods (*FPAR*-based and i_0-
347 based) for calculating total *SIF* have similar mean CVs of 14.2% (far-red) and 29.9% (red) for
348 wheat and 14.2% (far-red) and 24.6% (red) for corn, respectively. Overall, nadir *SIF* performs
349 similarly as total *SIF* in reducing the viewing angle effects. Using TOC reflectance instead of
350 $NIRv/Redv$ leads to similar results (Figure S2). Figure S2 shows that the relative SIF (calculated
351 as the ratio of raw *SIF* to reflected radiance) also has good performance in reducing the view-
352 angle effects, which is identical to the TROPOMI-based analysis reported by Magney et al.
353 (2019). Figure 4 shows the time series of half-hourly observed, nadir and total *SIFs*, and the
354 shaded areas of both nadir and total SIFs representing the standard deviations of *SIFs* are

355 generally narrower than raw observed SIF. This further demonstrates that both nadir and total
356 SIFs reduce the viewing-angle effects, when compared to raw *SIF* observations.

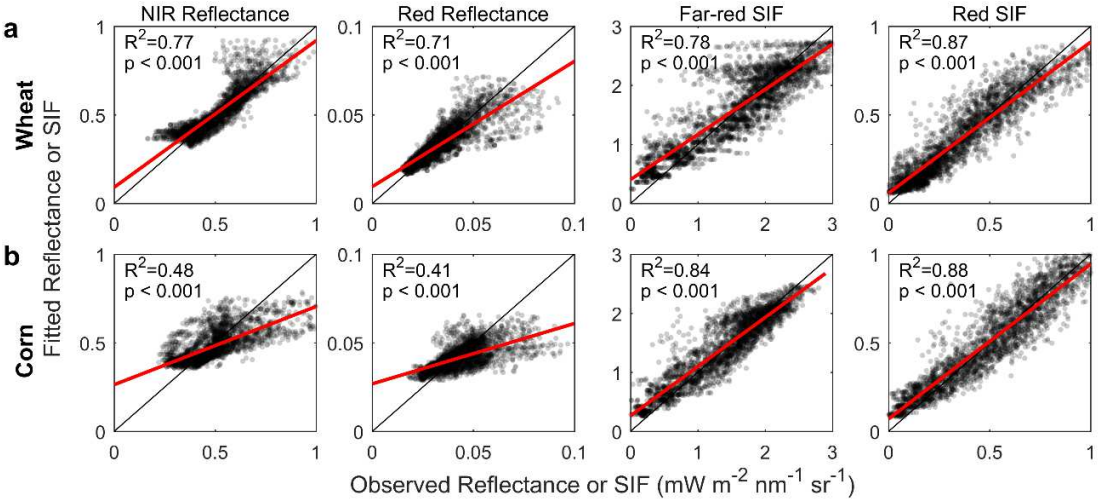

357

358 **Figure 2.** Comparison between observed and fitted reflectance and *SIF* values with the kernel-
359 driven model for red and far-red bands for **(a)** wheat and **(b)** corn. In each subplot, the degree of
360 transparency for each point represents the data density from low (white) to high (black); the red
361 line represents the linear regression line; and the R^2 and p-values of the linear fitting are also
362 presented**.**

363

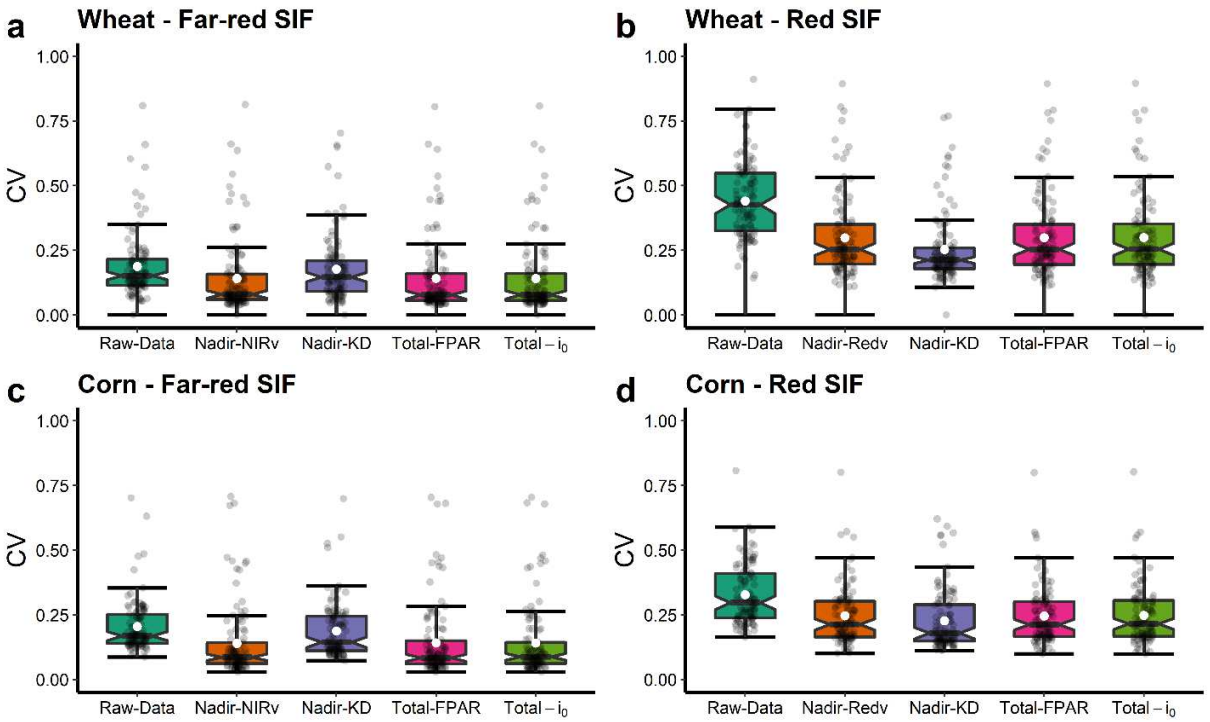

Figure 3. The coefficient of variation (CV) for observed/nadir/total *SIF*s for far-red and red bands for wheat (a-b) and corn (c-d). Here, CVs were calculated from each group of *SIF* values with the same *VZA* but different *VAA*s, where the raw observed data were acquired at a short time window of about 30 min. 'Raw-data', 'Nadir-NIRv/Redv', 'Nadir-KD', 'Total-FPAR' and 'Total-i_0' represent the raw observed *SIF*, nadir *SIF*s normalized by *NIRv*/*Redv*- and the KD-based methods, and total *SIF*s calculated by *FPAR*- or i_0-based methods, respectively. For each boxplot, white circles represent the mean values; the central lines represent the median values; boxes represent the interquartile ranges of the 25th (Q_{25}) and 75th (Q_{75}) percentiles; whiskers represent the values of Q_{25}-1.5*(Q_{75}-Q_{25}) and Q_{75}+1.5*(Q_{75}-Q_{25}); and grey points represent all CV values, whose degree of transparency represents the data density from low (white) to high (black).

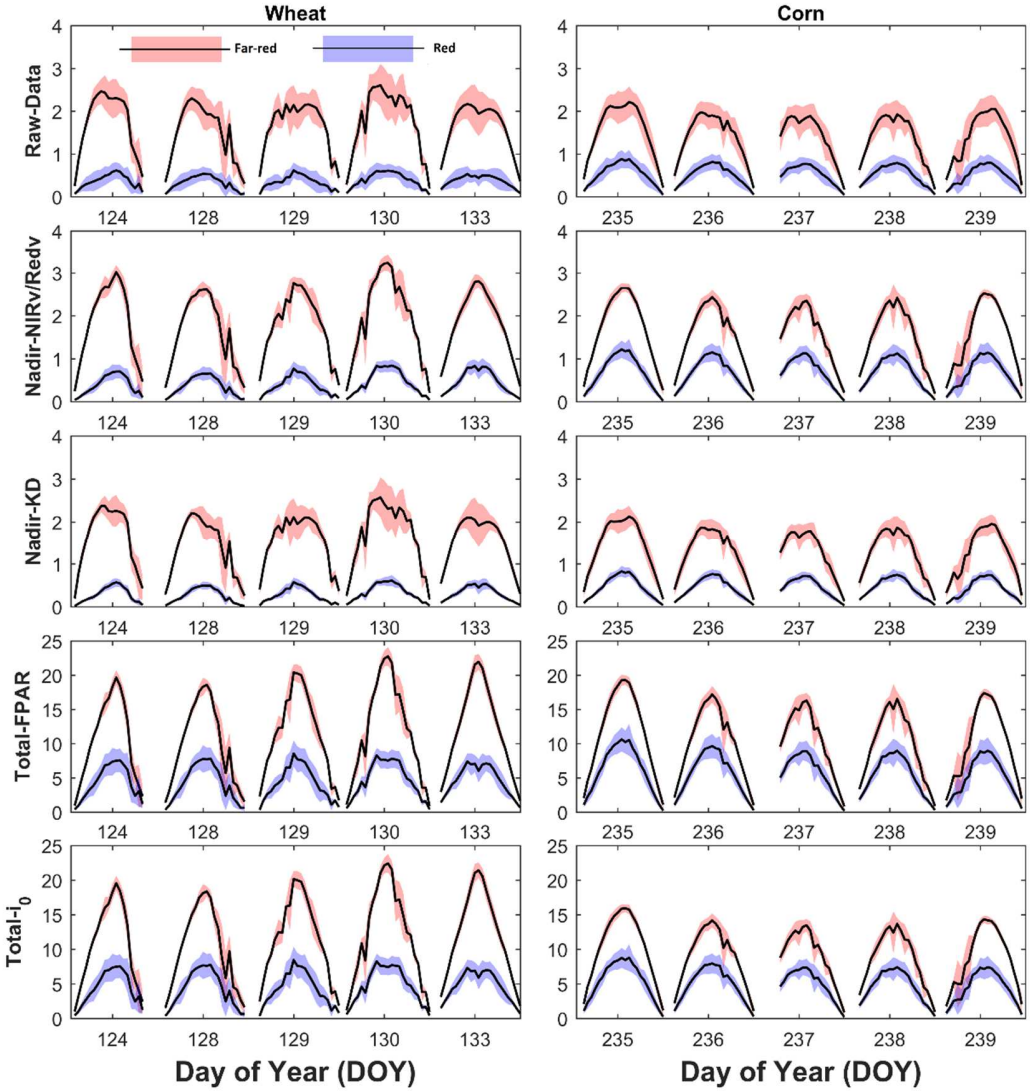

Figure 4. Time series of half-hourly raw observed, nadir and total SIFs (mW m^{-2} nm^{-1} (sr^{-1})) from 6:00-17:30 (UTC+8) in 2018, for wheat and corn. The black lines and shaded areas represent the mean and standard deviations of *SIF* values, every 30 min.

3.2 *SIF-GPP* relationship based on multi-angular field measurements at sub-daily scale

SIF_{nadir} is better correlated to GPP than observed multi-angular SIF_{obs} (Figure 5), due to the reduced viewing-angle effects (Section 3.1). For the linear relationship, when the *VAA* is fixed to be 240° and varying *VZA* (as a case), SIF_{obs} has R^2 values of 0.68 (far-red) and 0.35 (red) in wheat, and 0.59 (far-red) and 0.36 (red) in corn, respectively, while SIF_{nadir} normalized by the $NIRv/Redv$-based method has R^2 values of 0.78 (far-red) and 0.60 (red) in wheat and 0.68 (far-red) and 0.66 (red) in corn; and SIF_{nadir} normalized by the KD-based method has R^2 values of 0.77 (far-red) and 0.68 (red) in wheat and 0.74 (far-red) and 0.78 (red) in corn (see Figure 5). For all cases of *VAA* in Figure 6, SIF_{obs} has mean R^2 values of 0.66 (far-red) and 0.37 (red) in wheat and 0.60 (far-red) and 0.53 (red) in corn; the $NIRv/Redv$-based method has mean R^2 values of 0.73 (far-red) and 0.52 (red) in wheat and 0.64 (far-red) and 0.64 (red) in corn; and the KD-based method has mean R^2 values of 0.70 (far-red) and 0.58 (red) in wheat and 0.65 (far-red) and 0.63 (red) in corn. The improvements (i.e., the increases of R^2 value, ΔR^2) of SIF_{nadir} estimated by the two viewing angle normalization methods can reach up to 0.27 (far-red) and 0.31 (red) in wheat, and 0.18 (far-red) and 0.28 (red) in corn (see Figure S3). Specifically, for wheat, the ΔR^2 values for the KD-based method vary from -0.01 to 0.10 for far-red band with an average value of 0.04, and from 0.02 to 0.49 with an average value of 0.20 for red band; and the ΔR^2 values for corn vary from -0.09 to 0.35 for far-red band with an average value of 0.10 and from -0.06 to 0.17 for red band with an average value of 0.05 (Figure S3). The hyperbolic model generally has smaller RMSEs than linear model, especially for the red band in wheat, but SIF_{nadir} has smaller RMSEs than SIF_{obs} for the two models (Figures 5 and S4-S5).

SIF_{nadir} shows comparable performance for estimating GPP to SIF_{total}. The $FPAR$-based and i_0-based methods of calculating SIF_{total} achieve very similar results. Here we only

report the results of SIF_{total} calculated based on *FPAR*. For the linear relationship, when *VAA* is 240°, SIF_{total} has R^2 values of 0.76 (far-red) and 0.63 (red) in wheat, and 0.69 (far-red) and 0.66 (red) in corn, which are similar to SIF_{nadir} results (Figure 5). For all cases of *VAA* shown in Figure 6, the mean R^2 values are 0.69 (far-red) and 0.59 (red) in wheat, and 0.64 (far-red) and 0.63 (red); and the ΔR^2 values for SIF_{total} are similar to those for SIF_{nadir} (Figure 3). For RMSE, SIF_{nadir} and SIF_{total} still hold the similar results for linear and hyperbolic models (see Figures 6 and S4-S5).

411

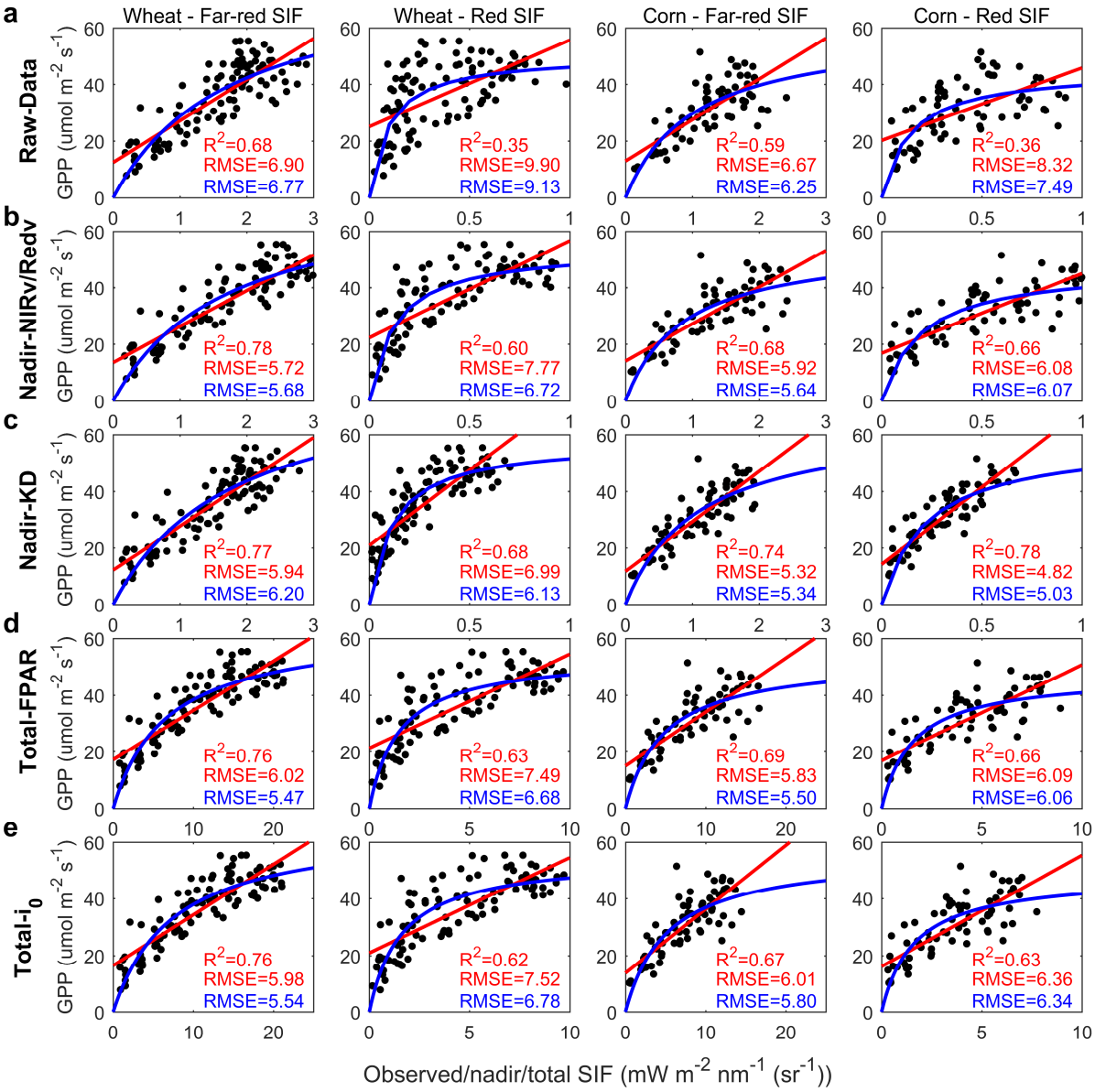

412

413 **Figure 5.** Performance of observed/nadir/total *SIF*s for far-red and red bands in predicting *GPP*
414 under the *VAA* of 240° but varying *VZA*s for wheat and corn. In each subplot, the red and blue
415 lines represent the linear and hyperbolic fitting lines, respectively; and R^2 and RMSEs of linear
416 fitting are marked by red colors, and RMSEs of hyperbolic fitting are marked by blue colors; p-
417 values are not included because they are smaller than 0.05 in all cases**.**

418

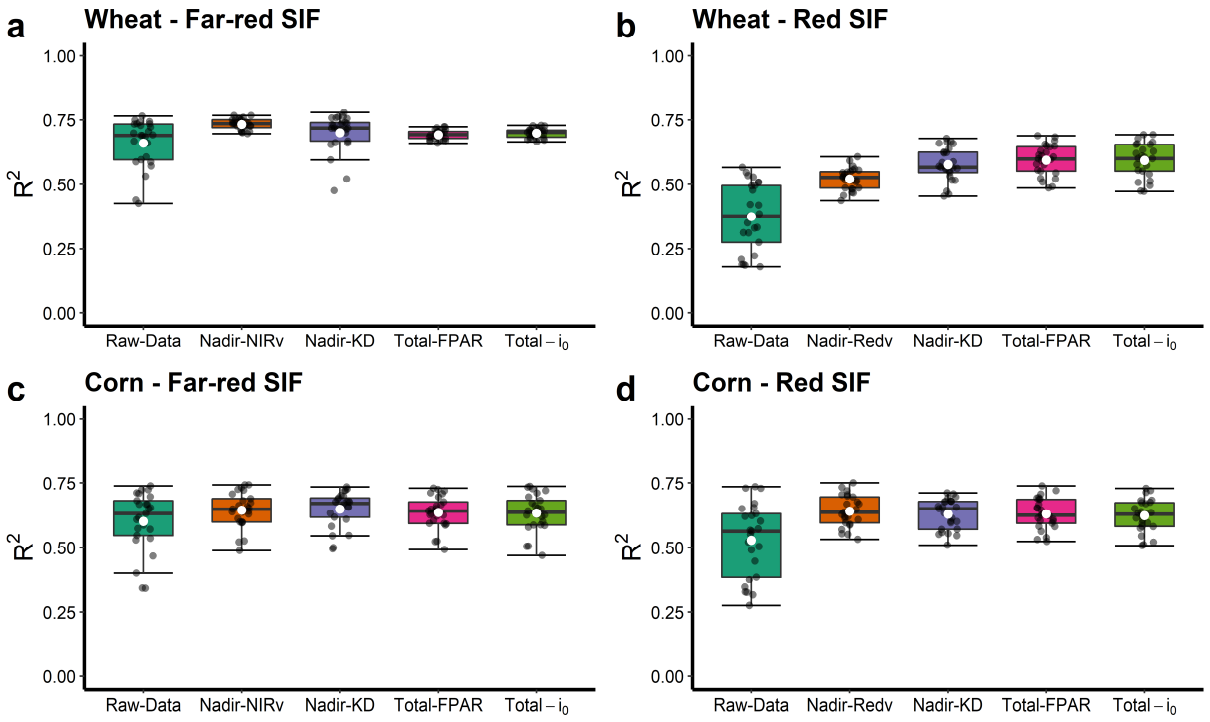

419

420 **Figure 6. The** R^2 values for the linear relationships between observed/nadir/total *SIF*s for far-red
421 and red bands and *GPP* under different *VAA*s for wheat (a-b) and corn (c-d). For each boxplot,
422 white circles represent the mean values and grey points represent R^2 values.

423

424

3.3 f_{esc} explains the different performance of SIF_{total} and SIF_{nadir}

As shown in Equation 2, the SIF photon escape ratio in the viewing angle, f_{esc}, represents the differences between SIF_{nadir} and SIF_{total}. Thus the relative performance of SIF_{nadir} and SIF_{total} on approximating *GPP* depends on how well f_{esc} is correlated with *LUE*. Figure 7 shows that nadir f_{esc} at the far-red wavelength has a strong positive correlation to *LUE*, which is consistent with results reported by Dechant et al., (2020). This explains why SIF_{nadir} is slightly better than SIF_{total} in Figures 5-6. However, the red f_{esc} is weakly or even negatively correlated with *LUE*, resulting that SIF_{nadir} is slightly inferior compared to SIF_{total} (Figures 5-6). It is worth noting that Equations 7-8 are empirical approximations and large uncertainties remain in calculating red f_{esc} (Liu et al., 2020) due to the large differences between leaf reflectance and transmittance in red band (Van der Tol et al., 2019; Yang et al., 2020).

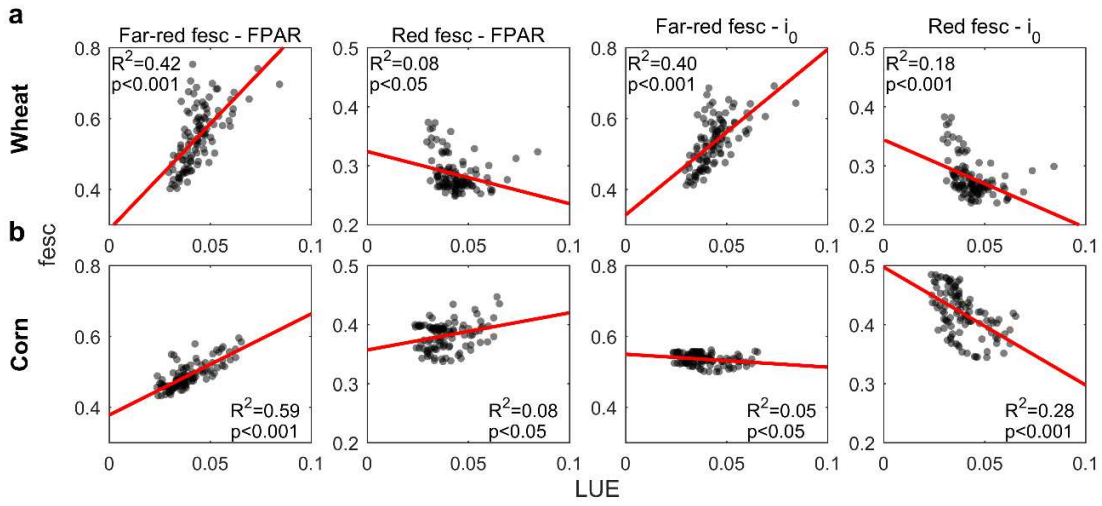

Figure 7. The relationships between *LUE* and nadir f_{esc} at the far-red and red wavelengths for (a) wheat and (b) corn. Here, 'f_{esc}-FPAR' and 'f_{esc}-i_0' represent the derived *fesc* values by *FPAR*- and i_0 -based methods. In each subplot, the degree of transparency of each point represents the data density from low (white) to high (black); the red line represents the linear regression line; and both R^2 values and *p*-values of linear relationships are also presented**.**

442

443 **3.4 Applications to daily TROPOMI data**

444 Overall, the TROPOMI far-red SIF_{nadir} has higher correlations to AmeriFlux *GPP* than
445 SIF_{obs} and shows similar performance with SIF_{total} for different PFTs, except MF and OSH
446 (Figure 8). Both SIF_{nadir} and SIF_{total} improved instantaneous *SIF-GPP* relationship at most of
447 the study sites, and the improvement of R^2 and RMSE (i.e., ΔR^2 and ΔRMSE) can exceed 0.1
448 and 1 umol·m^{-2}·s^{-1} at several sites for ENF and CRO. Specifically, with the *KD*-based method,
449 the ΔR^2 values of all ENF sites vary from -0.13 to 0.21 and its average value is 0.05; and the ΔR^2
450 values for CRO vary from -0.01 to 0.11 with an average value of 0.05. However, after correcting
451 to SIF_{nadir} and SIF_{total}, the *SIF-GPP* relationship becomes weaker at a few sites. For example,
452 for the *KD*-based method, the ΔR^2 values of all GRA sites vary from -0.18 to 0.10 and its
453 average value is 0.02. With the daily values, the improvements in R^2 and RMSE can exceed 0.2
454 and 1 gC·m^{-2}·day^{-1} at several CRO sites. Specifically, with the *KD*-based method, the ΔR^2 values
455 at ENF sites vary from -0.16 to 0.24 with an average value of 0.06; and the ΔR^2 values at CRO
456 sites vary from -0.01 to 0.18 with an average value of 0.06; and at GRA sites they vary from -
457 0.19 to 0.18 and with average value of 0.02. Different viewing angle normalization methods
458 generally show similar performance, but *NIRv*/*Redv*-based method performs the best for MF; the
459 KD-based method performs the best for ENF and CRO; and *FPAR*-based and i_0-based methods
460 has better performance for sparse vegetation canopies (i.e., OSH, WSA and GRA). Overall, the
461 results from our analyses of using only homogeneous sites (Figure S6) are similar to those using
462 all study sites (Figure 8). In addition, Figures 8 and S7-S8 show that using different cloud
463 fractions thresholds (i.e., 0.2, 0.5 and 0.8) has minimal impact on the results.

464

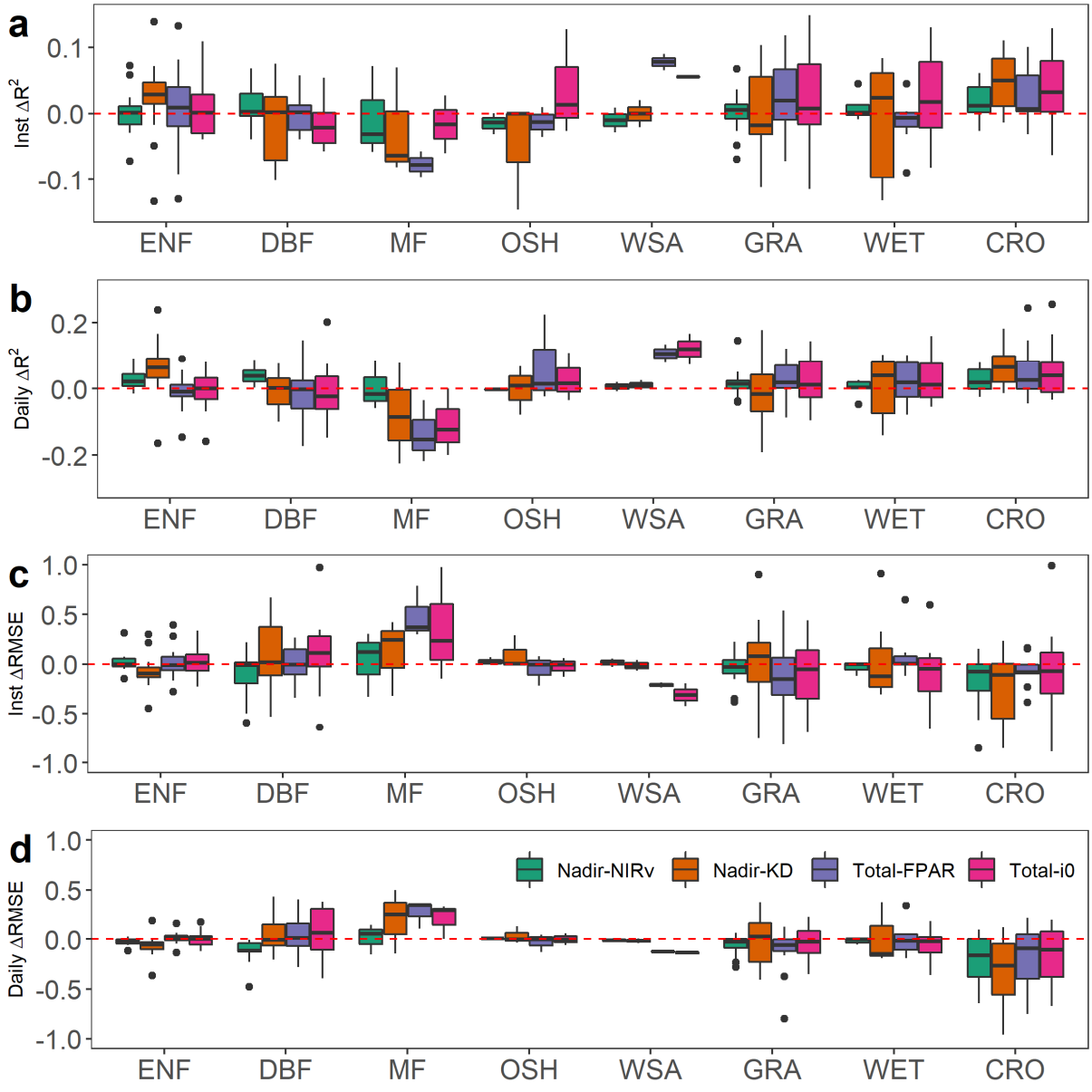

465

466 **Figure 8.** Changes in goodness of fit (ΔR^2 and ΔRMSE) for the linear fitting between TROPOMI

467 far-red *SIF* and AmeriFlux *GPP* after normalizing observed *SIF*s to nadir or total *SIF*s for all

468 sites with different PFTs. The units of ΔRMSE for instantaneous and daily scales are $umol \cdot m^{-2} \cdot s^{-1}$

469 and $gC \cdot m^{-2} \cdot day^{-1}$, respectively.

470

4 Discussion

SIF_{nadir} shows better performance than raw multi-angular *SIF* observations and it has comparable performance as SIF_{total} in estimating *GPP* at both sub-daily and daily scales. Compared to SIF_{obs} with varying viewing angles, both SIF_{nadir} and SIF_{total} effectively reduce the viewing-angle effects (Section 3.1). This explains why SIF_{total} shows better correlations to *GPP* as reported by Zhang et al. (2019, 2020b, 2020c). Furthermore, even if we adjusted the raw observations to a fixed off-nadir viewing angle (e.g., *VZA*=40°) following Lu et al., 2020, both SIF_{nadir} and SIF_{total} are still better correlated to *GPP* (Figure S9). This is likely because SIF_{obs} for an off-nadir angle can be subject to hotspot effects due to solar angle changes, while both SIF_{nadir} and SIF_{total} are less affected by hotspot effects. However, *SIF*s for different viewing angles can convey extra useful information about vegetation canopies. Off-nadir *SIF* measurements may work better at the beginning of the growing season, during which off-nadir sensors receive less soil background (Li et al., 2020). How to make full use of these complementary multi-angular *SIF* data to improve the *GPP* estimations deserves further investigations. It is worth noting that the KD-based method requires high-quality multi-angular *SIF* data but not f_{esc}, and shows better performance in red band than the *NIRv*/*Redv*-based method (Figures 3 and 5). However, the performance of the KD model is sensitive to the errors and uncertainties of the input *SIF* data (Figure 2), which likely account for its relatively worse performance in far-red band for wheat (Figure 6), indicating the necessity of reducing the uncertainties of *SIF* retrievals (Chang et al., 2020). The assumptions of constant vegetation structure and Φ_F stands in most cases with sufficient SIF measurements in a short time period, but attentions should be called when the period is long enough or at particular vegetation growing stages, e.g., the early growing season when the plants change rapidly. This method also

494 depends on the choice of kernels in the KD model (Hao et al., 2021b), whose performance needs
495 to be evaluated comprehensively before application.

496 In concept, SIF_{total} further reduces the scattering/reabsorption effects in addition to the
497 viewing-angle effects, but the correlation between *LUE* and f_{esc} is the key to determine the
498 different performance of SIF_{nadir} and SIF_{total} in approximating GPP (Dechant et al., 2020;
499 Figure 7). This finding explains the divergent conclusions and debates on the whether SIF_{total} or
500 SIF_{obs} better approximates GPP in previous studies. However, estimating SIF_{total} requires
501 accurate information about canopy structure parameters, while normalizing SIF_{obs} to nadir
502 viewing can be achieved using only reflectance or *SIF* data. Recently, a series of global-scale
503 *PAR*, $FPAR$, *LAI* and *CI* datasets have been produced (Hao et al., 2019; Hao et al., 2020a; He et
504 al., 2012; Myneni et al., 2002a; Wei et al., 2019), while their uncertainties are widely recognized
505 but usually not well quantified (Fang et al., 2019; Pisek et al., 2015; Zhang et al., 2020d). There
506 is no global *LAD* dataset available yet and a simplified assumption of spherical distribution or
507 prescribed biome-specific *LAD*s can introduce additional uncertainties. Accounting for the
508 spatio-temporal variations of ω especially for red band and the effects of diffuse skylight are
509 necessary for estimating SIF_{total} in global applications (Lu et al., 2020).

510 The relative *SIF* (the ratio of *SIF* to reflected radiance) also has good performance in
511 reducing the view-angle effects (Figure S2; Magney et al., 2019). However, because the relative
512 *SIF* is calculated as the ratio of *SIF* to reflected radiance, it has a different unit from *SIF* and does
513 not contain the *PAR* information. In fact, the relative *SIF* is proportional to Φ_F (Zeng et al.,
514 2019), which is promising for capturing the physiological response of vegetation to abiotic
515 changes and stresses.

Although overall performance of different methods to angular-normalizing TROPOMI *SIF* data were similar (Figure 8), small differences can be found due to divergent assumptions of the model/method as well as the quality and accuracy of remote sensing data. Compared to the two methods for estimating SIF_{total}, the two methods for estimating SIF_{nadir} do not rely on any inputs of canopy structure parameters and thus they should be more rubust across PFTs. The $NIRv$-based method was derived from Equations 5-6, and thus its performance relies on how well *NIRv* can approximate the true NIR reflectance of vegetation (Zeng et al., 2021). Zeng et al. (2021) developed a simple framework for estimating the true *NIRv* from hyperspectral data (NIRvH) with minimized soil contamination, which could be a promising approach for further improving the performance of this method for sparse vegetation canopies. In theory, the KD-based method is suitable for any PFT if the high-quality *SIF* data is available. However, this method shows poor performance over OSH, WSA and GRA (Figure 8), possibly due to the large relative errors of *SIF* retrievals for sparse vegetation canopies. For the methods of estimating SIF_{total}, in principle, the *FPAR*-based method can be applied for both dense and sparse vegetation canopies, while the i_0-based method is primarily suitable for dense canopies. For example, *FPAR*-based method performs the best over WSA for the instantaneous *SIFs*. The fact that these two methods show overall similar performance in our study is possibly due to the uncertainties of canopy structure parameters. Compared to the i_0-based method, the *FPAR*-based method only requires the input of *FPAR*, which is easier to acquire but its accuracy require further improvement (Zhang et al., 2020d). Overall, the *SIF* data quality and canopy structure parameters play important roles and may limit their applications in the performance for different PFTs, although the field measurement-based analysis shows that these methods work well for nearly all cases for wheat and corn canopies in this study (Figures 6 and S3).

539 We also used both linear and hyperbolic models to test the *SIF-GPP* relationship with
540 and without viewing angle normalizations. The hyperbolic model generally has higher R^2 values
541 than the linear model (Figure 5), because LUE can be expressed more realistically as a
542 hyperbolic function of absorbed *PAR* (Damm et al., 2015). This emphasizes the importance of
543 underlying assumptions associated with the model used when evaluating the *SIF-GPP*
544 relationship.

545 Our results highlight the necessity and feasibility of viewing angle normalization when
546 estimating *GPP* using remotely sensed *SIF*. The two methods for estimating SIF_{nadir} are
547 applicable to TROPOMI data, and SIF_{nadir} from TROPOMI shows a stronger relationship with
548 AmeriFlux *GPP* for most PFTs as compared with SIF_{obs}. These results are not sensitive to the
549 cloud cover (Figures 7 and S6-S7), confirming the robustness of the methods. In addition, most
550 of the existing remote sensing *SIF* data have a varying or off-nadir viewing angle. For example,
551 GOME-2 has a *VZA* of up to 54°; both OCO-2 and OCO-3 (Taylor et al., 2020) have large
552 viewing angles at glint and target modes; and the Geostationary Carbon Observatory (GeoCarb)
553 (Moore III et al., 2018) will have large off-nadir viewing angles over the high-latitude regions.
554 To better estimate *GPP*, the viewing-angle effects of *SIF* observations need to be minimized
555 first. Normalizing *SIF* observations to nadir viewing provides a promising way which can avoid
556 the effects of the uncertainties of vegetation canopy parameters. Although simply averaging *SIF*
557 observations over space and time can reduce the viewing angle effects, our study shows the
558 feasibility of viewing angle normalized nadir *SIF* with high spatio-temporal resolutions without a
559 need for any space-time smoothing. However, the footprints of TROPOMI can be large if the
560 *SIF* observations are from the edge of the swath, which may not be representative for the
561 dominant PFT of an eddy covariance tower site. Our results confirm that, our methods can

562 generally work well for both heterogenerous and homogenous study sites (Figures 7 and S6).
563 The spatial mismatch issues between TROPOMI, MODIS, and AmeriFlux data, spatial
564 heterogeneities and the representativeness of eddy-flux footprints for the tower sites (Chu et al.,
565 2021), may explain the degraded performance of normalized *SIF* for some PFTs (Figure 8). This
566 issue merits further investigations.

567 There are still a few limitations in our study. The field datasets we used only cover a
568 short period of a few days of observations and for homogeneous canopies. Using field
569 measurements for the entire growing season, or multiple seasons, over sparse canopies are
570 needed to further evaluate robustness of our proposed methodology. The multi-angular
571 measurements in the study were acquired by dynamically rotating the optical probe, which
572 means the target footprint under different viewing angles was different. The measurements did
573 not cover the full principal (PP) and cross-principal (CPP) planes and thus cannot capture
574 completely the BRDF shapes in PP and CPP. The spectrometer used to obtain the field
575 measurements had a large FOV of 25°, which may lead to uncertainties in the measured multi-
576 angular data. Although TROPOMI data provide unprecedented temporal resolutions, satellite-
577 based *SIF* retrievals are still noisy and have high relative uncertainties for red band (Köhler et al.,
578 2020). Further improving the quality of satellite-based *SIF* retrievals are required for detailed
579 quantitative analysis and applications. In addition, TROPOMI *SIF* data still have sparse spatial
580 resolution, which are hopefully resolved by future missions, such as GeoCarb and the
581 forthcoming Fluorescence Explorer (FLEX) mission of the European Space Agency (Kraft et al.,
582 2017).

583

5 Conclusions

Directional effects of *SIF* measurements greatly hinder the robust estimation of *GPP*. In this study, we used two practical methods to normalize *SIF* observations to nadir viewing, and used two simple methods to calculate the total *SIF*. We used the multi-angular field measurements for wheat and corn at sub-daily scale, TROPOMI *SIF* and AmeriFlux *GPP* data at daily scale to evaluate their relationships with *GPP*. Our results show that, overall, the four methods show good performance in reducing the viewing angle effects on *SIF*. Nadir *SIF* can better track *GPP* than raw multi-angular observations, due to the reduced viewing angle effects. Nadir *SIF* also shows comparable performance with total *SIF*, but estimating nadir *SIF* only requires reflectance or *SIF* observations, rather than detailed canopy structure parameters generally needed for estimated total *SIF*. The varying relationship of *LUE* and f_{esc} can account for the relative performance of nadir and total *SIF*s on approximating *GPP*. Our results underline the significance, effectiveness and feasibility of using normalized nadir *SIF* to better estimate *GPP,* especially over large areas.

Acknowledgments

This research was supported a Laboratory Directed Research and Development project sponsored by the Pacific Northwest National Laboratory (PNNL) of the U.S. Department of Energy to Min Chen. PNNL is operated by Battelle for the U.S. Department of Energy under Contract DE-AC05-76RL01830. Khelvi Biriukova, Marco Celesti, and Micol Rossini were supported by the European Union's Horizon 2020 research and innovation programme under the Marie Skłodowska-Curie grant agreement No. 721995. Marco Celesti was supported by a Living

606 Planet Fellowship (ESA/Contract No. 4000125442/18/I-NS) of the European Space Agency.
607 Multi-angular field data is available through https://doi.org/10.6084/m9.figshare.13011470.v2.
608 We thank Mirco Migliavacca for his contribution to the viewing angle-normalization methods.
609 We acknowledge the AmeriFlux community for sharing the flux data (available at
610 https://ameriflux.lbl.gov/). We also acknowledge Philipp Köhler and Christian Frankenberg for
611 providing useful suggestions and TROPOMI SIF data (available at
612 ftp://fluo.gps.caltech.edu/data/tropomi/). All MODIS data are available from GEE. Codes to
613 reproduce all results are available at https://github.com/daleihao/SIFNormalization.
614

References

Asner, G.P., 1998. Biophysical and Biochemical Sources of Variability in Canopy Reflectance. Remote Sensing of Environment 64, 234-253.

Badgley, G., Field, C.B., Berry, J.A., 2017. Canopy near-infrared reflectance and terrestrial photosynthesis. Science Advances 3, e1602244.

Belward, A.S., Estes, J.E., Kline, K.D., 1999. The IGBP-DIS global 1-km land-cover data set DISCover: A project overview. Photogrammetric Engineering and Remote Sensing 65, 1013-1020.

Biriukova, K., Celesti, M., Evdokimov, A., Pacheco-Labrador, J., Julitta, T., Migliavacca, M., Giardino, C., Miglietta, F., Colombo, R., Panigada, C., 2020. Effects of varying solar-view geometry and canopy structure on solar-induced chlorophyll fluorescence and PRI. International Journal of Applied Earth Observation Geoinformation 89, 102069.

Chang, C.Y., Guanter, L., Frankenberg, C., Köhler, P., Gu, L., Magney, T.S., Grossmann, K., Sun, Y., 2020. Systematic Assessment of Retrieval Methods for Canopy Far-Red Solar-Induced Chlorophyll Fluorescence Using High-Frequency Automated Field Spectroscopy. Journal of Geophysical Research: Biogeosciences 125, e2019JG005533.

Chen, J.M., Leblanc, S.G., 2001. Multiple-scattering scheme useful for geometric optical modeling. IEEE Transactions on Geoscience Remote Sensing 39, 1061-1071.

Cogliati, S., Verhoef, W., Kraft, S., Sabater, N., Alonso, L., Vicent, J., Moreno, J., Drusch, M., Colombo, R., 2015. Retrieval of sun-induced fluorescence using advanced spectral fitting methods. Remote sensing of environment 169, 344-357.

Damm, A., Guanter, L., Paul-Limoges, E., Van der Tol, C., Hueni, A., Buchmann, N., Eugster, W., Ammann, C., Schaepman, M.E., 2015. Far-red sun-induced chlorophyll fluorescence shows ecosystem-specific relationships to gross primary production: An assessment based on observational and modeling approaches. Remote Sensing of Environment 166, 91-105.

Dechant, B., Ryu, Y., Badgley, G., Zeng, Y., Berry, J.A., Zhang, Y., Goulas, Y., Li, Z., Zhang, Q., Kang, M.J.R.S.o.E., 2020. Canopy structure explains the relationship between photosynthesis and sun-induced chlorophyll fluorescence in crops. 241, 111733.

642 Doughty, R., Köhler, P., Frankenberg, C., Magney, T.S., Xiao, X., Qin, Y., Wu, X., Moore, B., 2019. TROPOMI
643 reveals dry-season increase of solar-induced chlorophyll fluorescence in the Amazon forest. Proceedings of the
644 National Academy of Sciences 116, 22393-22398.
645 Fang, H., Baret, F., Plummer, S., Schaepman-Strub, G., 2019. An overview of global leaf area index (LAI):
646 Methods, products, validation, and applications. Reviews of Geophysics 57, 739-799.
647 Frankenberg, C., Fisher, J.B., Worden, J., Badgley, G., Saatchi, S.S., Lee, J.-E., Toon, G.C., Butz, A., Jung, M.,
648 Kuze, A., Yokota, T., 2011. New global observations of the terrestrial carbon cycle from GOSAT: Patterns of plant
649 fluorescence with gross primary productivity. Geophysical Research Letters 38.
650 Frankenberg, C., O'Dell, C., Berry, J., Guanter, L., Joiner, J., Köhler, P., Pollock, R., Taylor, T.E., 2014. Prospects
651 for chlorophyll fluorescence remote sensing from the Orbiting Carbon Observatory-2. Remote Sensing of
652 Environment 147, 1-12.
653 Friedl, M.A., McIver, D.K., Hodges, J.C., Zhang, X.Y., Muchoney, D., Strahler, A.H., Woodcock, C.E., Gopal, S.,
654 Schneider, A., Cooper, A., 2002. Global land cover mapping from MODIS: algorithms and early results. Remote
655 sensing of Environment 83, 287-302.
656 Gates, D.M., Keegan, H.J., Schleter, J.C., Weidner, V.R., 1965. Spectral Properties of Plants. Appl. Opt. 4, 11-20.
657 Gorelick, N., Hancher, M., Dixon, M., Ilyushchenko, S., Thau, D., Moore, R., 2017. Google Earth Engine:
658 Planetary-scale geospatial analysis for everyone. Remote Sensing of Environment 202, 18-27.
659 Grossmann, K., Frankenberg, C., Magney, T.S., Hurlock, S.C., Seibt, U., Stutz, J., 2018. PhotoSpec: A new
660 instrument to measure spatially distributed red and far-red Solar-Induced Chlorophyll Fluorescence. Remote Sensing
661 of Environment 216, 311-327.
662 Gu, L., Han, J., Wood, J.D., Chang, C.Y.Y., Sun, Y., 2019. Sun-induced Chl fluorescence and its importance for
663 biophysical modeling of photosynthesis based on light reactions. New Phytologist 223, 1179-1191.
664 Guan, K., Berry, J.A., Zhang, Y., Joiner, J., Guanter, L., Badgley, G., Lobell, D.B., 2016. Improving the monitoring
665 of crop productivity using spaceborne solar-induced fluorescence. Global change biology 22, 716-726.
666 Guanter, L., Frankenberg, C., Dudhia, A., Lewis, P.E., Gómez-Dans, J., Kuze, A., Suto, H., Grainger, R.G., 2012.
667 Retrieval and global assessment of terrestrial chlorophyll fluorescence from GOSAT space measurements. Remote
668 Sensing of Environment 121, 236-251.

669 Hao, D., Asrar, G.R., Zeng, Y., Yang, X., Li, X., Xiao, J., Guan, K., Wen, J., Xiao, Q., Berry, J.A., Chen, M., 2021a.
670 Potential of hotspot solar-induced chlorophyll fluorescence for better tracking terrestrial photosynthesis. Global
671 Change Biology 27, 2144-2158.
672 Hao, D., Asrar, G.R., Zeng, Y., Zhu, Q., Wen, J., Xiao, Q., Chen, M., 2019. Estimating hourly land surface
673 downward shortwave and photosynthetically active radiation from DSCOVR/EPIC observations. Remote Sensing of
674 Environment 232, 111320.
675 Hao, D., Asrar, G.R., Zeng, Y., Zhu, Q., Wen, J., Xiao, Q., Chen, M., 2020a. DSCOVR/EPIC-derived global hourly
676 and daily downward shortwave and photosynthetically active radiation data at $0.1^\circ \times 0.1^\circ$ resolution. Earth Syst. Sci.
677 Data 12, 2209-2221.
678 Hao, D., Wen, J., Xiao, Q., You, D., Tang, Y., 2020b. An Improved Topography-Coupled Kernel-Driven Model for
679 Land Surface Anisotropic Reflectance. IEEE Transactions on Geoscience and Remote Sensing 58, 2833-2847.
680 Hao, D., Zeng, Y., Qiu, H., Biriukova, K., Celesti, M., Migliavacca, M., Rossini, M., Asrar, G.R., Chen, M., 2021b.
681 Practical approaches for normalizing directional solar-induced fluorescence to a standard viewing geometry. Remote
682 Sensing of Environment 255, 112171.
683 He, L., Chen, J.M., Liu, J., Mo, G., Joiner, J., 2017. Angular normalization of GOME-2 Sun-induced chlorophyll
684 fluorescence observation as a better proxy of vegetation productivity. Geophysical Research Letters 44, 5691-5699.
685 He, L., Chen, J.M., Pisek, J., Schaaf, C.B., Strahler, A.H., 2012. Global clumping index map derived from the
686 MODIS BRDF product. Remote Sensing of Environment 119, 118-130.
687 He, L., Magney, T., Dutta, D., Yin, Y., Köhler, P., Grossmann, K., Stutz, J., Dold, C., Hatfield, J., Guan, K., Peng,
688 B., Frankenberg, C., 2020a. From the Ground to Space: Using Solar-Induced Chlorophyll Fluorescence to Estimate
689 Crop Productivity. Geophysical Research Letters 47, e2020GL087474.
690 He, L., Wood, J.D., Sun, Y., Magney, T., Dutta, D., Köhler, P., Zhang, Y., Yin, Y., Frankenberg, C., 2020b.
691 Tracking seasonal and interannual variability in photosynthetic downregulation in response to water stress at a
692 temperate deciduous forest. Journal of Geophysical Research: Biogeosciences 125, e2018JG005002.
693 Joiner, J., Yoshida, Y., Vasilkov, A.P., Yoshida, Y., Corp, L.A., Middleton, E.M., 2011. First observations of global
694 and seasonal terrestrial chlorophyll fluorescence from space. Biogeosciences 8, 637-651.

695 Köhler, P., Behrenfeld, M.J., Landgraf, J., Joiner, J., Magney, T.S., Frankenberg, C., 2020. Global Retrievals of
696 Solar-Induced Chlorophyll Fluorescence at Red Wavelengths With TROPOMI. Geophysical Research Letters 47,
697 e2020GL087541.
698 Köhler, P., Frankenberg, C., Magney, T.S., Guanter, L., Joiner, J., Landgraf, J., 2018. Global Retrievals of Solar-
699 Induced Chlorophyll Fluorescence With TROPOMI: First Results and Intersensor Comparison to OCO-2.
700 Geophysical Research Letters 45, 10,456-410,463.
701 Kraft, S., Del Bello, U., Harnisch, B., Bouvet, M., Drusch, M., Bézy, J.-L., 2017. Fluorescence imaging
702 spectrometer concepts for the earth explorer mission candidate flex, International Conference on Space Optics—
703 ICSO 2012. International Society for Optics and Photonics, p. 105641W.
704 Lee, J.-E., Frankenberg, C., van der Tol, C., Berry, J.A., Guanter, L., Boyce, C.K., Fisher, J.B., Morrow, E.,
705 Worden, J.R., Asefi, S., 2013. Forest productivity and water stress in Amazonia: Observations from GOSAT
706 chlorophyll fluorescence. Proceedings of the Royal Society B: Biological Sciences 280, 20130171.
707 Li, D., Chen, J.M., Zhang, X., Yan, Y., Zhu, J., Zheng, H., Zhou, K., Yao, X., Tian, Y., Zhu, Y., Cheng, T., Cao,
708 W., 2020. Improved estimation of leaf chlorophyll content of row crops from canopy reflectance spectra through
709 minimizing canopy structural effects and optimizing off-noon observation time. Remote Sensing of Environment
710 248, 111985.
711 Li, X., Gao, F., Chen, L., Strahler, A.H., 1999. Derivation and validation of a new kernel for kernel-driven BRDF
712 models, Remote Sensing for Earth Science, Ocean, and Sea Ice Applications. International Society for Optics and
713 Photonics, pp. 368-379.
714 Liu, L., Liu, X., Wang, Z., Zhang, B., 2015. Measurement and analysis of bidirectional SIF emissions in wheat
715 canopies. IEEE Transactions on Geoscience Remote Sensing 54, 2640-2651.
716 Liu, X., Guanter, L., Liu, L., Damm, A., Malenovský, Z., Rascher, U., Peng, D., Du, S., Gastellu-Etchegorry, J.-P.,
717 2019. Downscaling of solar-induced chlorophyll fluorescence from canopy level to photosystem level using a
718 random forest model. Remote sensing of environment 231, 110772.
719 Liu, X., Liu, L., Hu, J., Guo, J., Du, S., 2020. Improving the potential of red SIF for estimating GPP by downscaling
720 from the canopy level to the photosystem level. Agricultural Forest Meteorology 281, 107846.
721 Lu, X., Liu, Z., An, S., Miralles, D.G., Maes, W., Liu, Y., Tang, J., 2018. Potential of solar-induced chlorophyll
722 fluorescence to estimate transpiration in a temperate forest. Agricultural and Forest Meteorology 252, 75-87.

723 Lu, X., Liu, Z., Zhao, F., Tang, J., 2020. Comparison of total emitted solar-induced chlorophyll fluorescence (SIF)
724 and top-of-canopy (TOC) SIF in estimating photosynthesis. Remote Sensing of Environment 251, 112083.
725 Maes, W.H., Pagán, B.R., Martens, B., Gentine, P., Guanter, L., Steppe, K., Verhoest, N.E., Dorigo, W., Li, X.,
726 Xiao, J., 2020. Sun-induced fluorescence closely linked to ecosystem transpiration as evidenced by satellite data and
727 radiative transfer models. Remote Sensing of Environment 249, 112030.
728 Magney, T.S., Barnes, M.L., Yang, X., 2020. On the Covariation of Chlorophyll Fluorescence and Photosynthesis
729 Across Scales. Geophysical Research Letters 47, e2020GL091098.
730 Magney, T.S., Bowling, D.R., Logan, B.A., Grossmann, K., Stutz, J., Blanken, P.D., Burns, S.P., Cheng, R., Garcia,
731 M.A., Köhler, P., Lopez, S., Parazoo, N.C., Raczka, B., Schimel, D., Frankenberg, C., 2019. Mechanistic evidence
732 for tracking the seasonality of photosynthesis with solar-induced fluorescence. Proceedings of the National
733 Academy of Sciences 116, 11640.
734 Meroni, M., Rossini, M., Guanter, L., Alonso, L., Rascher, U., Colombo, R., Moreno, J., 2009. Remote sensing of
735 solar-induced chlorophyll fluorescence: Review of methods and applications. Remote Sensing of Environment 113,
736 2037-2051.
737 Mohammed, G.H., Colombo, R., Middleton, E.M., Rascher, U., van der Tol, C., Nedbal, L., Goulas, Y., Pérez-
738 Priego, O., Damm, A., Meroni, M., 2019. Remote sensing of solar-induced chlorophyll fluorescence (SIF) in
739 vegetation: 50 years of progress. Remote sensing of environment 231, 111177.
740 Moore III, B., Crowell, S.M., Rayner, P.J., Kumer, J., O'Dell, C.W., O'Brien, D., Utembe, S., Polonsky, I., Schimel,
741 D., Lemen, J., 2018. The potential of the geostationary Carbon Cycle Observatory (GeoCarb) to provide multi-scale
742 constraints on the carbon cycle in the Americas. Frontiers in Environmental Science 6, 109.
743 Myneni, R.B., Hoffman, S., Knyazikhin, Y., Privette, J., Glassy, J., Tian, Y., Wang, Y., Song, X., Zhang, Y., Smith,
744 G., 2002a. Global products of vegetation leaf area and fraction absorbed PAR from year one of MODIS data.
745 Remote sensing of environment 83, 214-231.
746 Myneni, R.B., Hoffman, S., Knyazikhin, Y., Privette, J.L., Glassy, J., Tian, Y., Wang, Y., Song, X., Zhang, Y.,
747 Smith, G.R., Lotsch, A., Friedl, M., Morisette, J.T., Votava, P., Nemani, R.R., Running, S.W., 2002b. Global
748 products of vegetation leaf area and fraction absorbed PAR from year one of MODIS data. Remote Sensing of
749 Environment 83, 214-231.

Pinto, F., Müller-Linow, M., Schickling, A., Cendrero-Mateo, M.P., Ballvora, A., Rascher, U., 2017. Multiangular observation of canopy sun-induced chlorophyll fluorescence by combining imaging spectroscopy and stereoscopy. Remote Sensing 9, 415.

Pisek, J., Govind, A., Arndt, S.K., Hocking, D., Wardlaw, T.J., Fang, H., Matteucci, G., Longdoz, B., 2015. Intercomparison of clumping index estimates from POLDER, MODIS, and MISR satellite data over reference sites. ISPRS Journal of Photogrammetry Remote Sensing 101, 47-56.

Reichstein, M., Falge, E., Baldocchi, D., Papale, D., Aubinet, M., Berbigier, P., Bernhofer, C., Buchmann, N., Gilmanov, T., Granier, A., Grünwald, T., Havránková, K., Ilvesniemi, H., Janous, D., Knohl, A., Laurila, T., Lohila, A., Loustau, D., Matteucci, G., Meyers, T., Miglietta, F., Ourcival, J.-M., Pumpanen, J., Rambal, S., Rotenberg, E., Sanz, M., Tenhunen, J., Seufert, G., Vaccari, F., Vesala, T., Yakir, D., Valentini, R., 2005. On the separation of net ecosystem exchange into assimilation and ecosystem respiration: review and improved algorithm. Global Change Biology 11, 1424-1439.

Rogers, C.A., Chen, J.M., Zheng, T., Croft, H., Gonsamo, A., Luo, X., Staebler, R.M., 2020. The Response of Spectral Vegetation Indices and Solar-Induced Fluorescence to Changes in Illumination Intensity and Geometry in the Days Surrounding the 2017 North American Solar Eclipse. Journal of Geophysical Research: Biogeosciences 125, e2020JG005774.

Roujean, J.L., Leroy, M., Deschamps, P.Y., 1992. A bidirectional reflectance model of the Earth's surface for the correction of remote sensing data. Journal of Geophysical Research: Atmospheres 97, 20455-20468.

Ryu, Y., Berry, J.A., Baldocchi, D.D., 2019. What is global photosynthesis? History, uncertainties and opportunities. Remote sensing of environment 223, 95-114.

Sakai, Y., Kobayashi, H., Kato, T., 2020. FLiES-SIF version 1.0: three-dimensional radiative transfer model for estimating solar induced fluorescence. Geoscientific Model Development 13, 4041-4066.

Schaaf, C.B., Gao, F., Strahler, A.H., Lucht, W., Li, X., Tsang, T., Strugnell, N.C., Zhang, X., Jin, Y., Muller, J.-P., Lewis, P., Barnsley, M., Hobson, P., Disney, M., Roberts, G., Dunderdale, M., Doll, C., d'Entremont, R.P., Hu, B., Liang, S., Privette, J.L., Roy, D., 2002. First operational BRDF, albedo nadir reflectance products from MODIS. Remote Sensing of Environment 83, 135-148.

776 Shan, N., Ju, W., Migliavacca, M., Martini, D., Guanter, L., Chen, J., Goulas, Y., Zhang, Y., 2019. Modeling canopy
777 conductance and transpiration from solar-induced chlorophyll fluorescence. Agricultural and Forest Meteorology
778 268, 189-201.
779 Shan, N., Zhang, Y., Chen, J.M., Ju, W., Migliavacca, M., Peñuelas, J., Yang, X., Zhang, Z., Nelson, J.A., Goulas,
780 Y., 2021. A model for estimating transpiration from remotely sensed solar-induced chlorophyll fluorescence.
781 Remote Sensing of Environment 252, 112134.
782 Song, L., Guanter, L., Guan, K., You, L., Huete, A., Ju, W., Zhang, Y., 2018. Satellite sun-induced chlorophyll
783 fluorescence detects early response of winter wheat to heat stress in the Indian Indo-Gangetic Plains. Global change
784 biology 24, 4023-4037.
785 Smolander, S., Stenberg, P., 2005. Simple parameterizations of the radiation budget of uniform broadleaved and
786 coniferous canopies. Remote Sensing of Environment 94, 355-363.
787 Sun, Y., Frankenberg, C., Wood, J.D., Schimel, D.S., Jung, M., Guanter, L., Drewry, D., Verma, M., Porcar-Castell,
788 A., Griffis, T.J., 2017. OCO-2 advances photosynthesis observation from space via solar-induced chlorophyll
789 fluorescence. Science 358.
790 Taylor, T.E., Eldering, A., Merrelli, A., Kiel, M., Somkuti, P., Cheng, C., Rosenberg, R., Fisher, B., Crisp, D.,
791 Basilio, R., 2020. OCO-3 early mission operations and initial (vEarly) XCO2 and SIF retrievals. Remote sensing of
792 environment 251, 112032.
793 Tucker, C.J., 1979. Red and photographic infrared linear combinations for monitoring vegetation. Remote Sensing
794 of Environment 8, 127-150.
795 Van der Tol, C., Vilfan, N., Dauwe, D., Cendrero-Mateo, M.P., Yang, P., 2019. The scattering and re-absorption of
796 red and near-infrared chlorophyll fluorescence in the models Fluspect and SCOPE. Remote sensing of environment
797 232, 111292.
798 Wang, C., Beringer, J., Hutley, L.B., Cleverly, J., Li, J., Liu, Q., Sun, Y., 2019. Phenology Dynamics of Dryland
799 Ecosystems Along the North Australian Tropical Transect Revealed by Satellite Solar-Induced Chlorophyll
800 Fluorescence. Geophysical Research Letters 46, 5294-5302.
801 Wang, C., Guan, K., Peng, B., Chen, M., Jiang, C., Zeng, Y., Wu, G., Wang, S., Wu, J., Yang, X., Frankenberg, C.,
802 Köhler, P., Berry, J., Bernacchi, C., Zhu, K., Alden, C., Miao, G., 2020. Satellite footprint data from OCO-2 and

803 TROPOMI reveal significant spatio-temporal and inter-vegetation type variabilities of solar-induced fluorescence
804 yield in the U.S. Midwest. Remote Sensing of Environment 241, 111728.
805 Wei, S., Fang, H., Schaaf, C.B., He, L., Chen, J.M., 2019. Global 500 m clumping index product derived from
806 MODIS BRDF data (2001–2017). Remote sensing of environment 232, 111296.
807 Wutzler, T., Lucas-Moffat, A., Migliavacca, M., Knauer, J., Sickel, K., Šigut, L., Menzer, O., Reichstein, M., 2018.
808 Basic and extensible post-processing of eddy covariance flux data with REddyProc. Biogeosciences 15, 5015-5030.
809 Yang, K., Ryu, Y., Dechant, B., Berry, J.A., Hwang, Y., Jiang, C., Kang, M., Kim, J., Kimm, H., Kornfeld, A.,
810 Yang, X., 2018. Sun-induced chlorophyll fluorescence is more strongly related to absorbed light than to
811 photosynthesis at half-hourly resolution in a rice paddy. Remote Sensing of Environment 216, 658-673.
812 Yang, P., Van der Tol, C., 2018. Linking canopy scattering of far-red sun-induced chlorophyll fluorescence with
813 reflectance. Remote sensing of environment 209, 456-467.
814 Yang, P., Van der Tol, C., Campbell, P.K., Middleton, E.M., 2020. Fluorescence Correction Vegetation Index
815 (FCVI): A physically based reflectance index to separate physiological and non-physiological information in far-red
816 sun-induced chlorophyll fluorescence. Remote sensing of environment 240, 111676.
817 Zeng, Y., Badgley, G., Chen, M., Li, J., Anderegg, L.D., Kornfeld, A., Liu, Q., Xu, B., Yang, B., Yan, K., 2020. A
818 radiative transfer model for solar induced fluorescence using spectral invariants theory. Remote Sensing of
819 Environment 240, 111678.
820 Zeng, Y., Badgley, G., Dechant, B., Ryu, Y., Chen, M., Berry, J.A., 2019. A practical approach for estimating the
821 escape ratio of near-infrared solar-induced chlorophyll fluorescence. Remote Sensing of Environment 232, 111209.
822 Zeng Y., Hao, D., Badgley, G., Damm, A., Rascher, U., Ryu, Y., Johnson, J., Krieger, V., Wu, S., Qiu, H., Berry,
823 J.A., Chen, M., 2021. Estimating near-infrared reflectance of vegetation from hyperspectral data. Remote Sensing of
824 Environment (Accepted).
825 Zhang, Q., Zhang, Y., Li, Z., Li, J., Zhang, X., 2019a. The effects of sun-viewer geometry on sun-induced
826 fluorescence and its relationship with gross primary production, IGARSS 2019-2019 IEEE International Geoscience
827 and Remote Sensing Symposium. IEEE, pp. 9048-9051.
828 Zhang, Q., Chen, J.M., Ju, W., Zhang, Y., Li, Z., He, L., Pacheco-Labrador, J., Li, J., Qiu, B., Zhang, X., Qiu, F.,
829 Chen, B., Chou, S., Zhang, Z., Shan, N., 2021. Ground-Based Multiangle Solar-Induced Chlorophyll Fluorescence

Observation and Angular Normalization for Assessing Crop Productivity. Journal of Geophysical Research: Biogeosciences 126, e2020JG006082.

Zhang, Y., Commane, R., Zhou, S., Williams, A.P., Gentine, P., 2020a. Light limitation regulates the response of autumn terrestrial carbon uptake to warming. Nature Climate Change 10, 739-743.

Zhang, Y., Xiao, X., Zhang, Y., Wolf, S., Zhou, S., Joiner, J., Guanter, L., Verma, M., Sun, Y., Yang, X., Paul-Limoges, E., Gough, C.M., Wohlfahrt, G., Gioli, B., van der Tol, C., Yann, N., Lund, M., de Grandcourt, A., 2018a. On the relationship between sub-daily instantaneous and daily total gross primary production: Implications for interpreting satellite-based SIF retrievals. Remote Sensing of Environment 205, 276-289.

Zhang, Z., Chen, J.M., Guanter, L., He, L., Zhang, Y.J.G.R.L., 2019b. From canopy-leaving to total canopy far-red fluorescence emission for remote sensing of photosynthesis: First results from TROPOMI. 46, 12030-12040.

Zhang, Z., Zhang, Y., Joiner, J., Migliavacca, M., 2018b. Angle matters: Bidirectional effects impact the slope of relationship between gross primary productivity and sun-induced chlorophyll fluorescence from Orbiting Carbon Observatory-2 across biomes. Global change biology 24, 5017-5020.

Zhang, Z., Zhang, Y., Porcar-Castell, A., Joiner, J., Guanter, L., Yang, X., Migliavacca, M., Ju, W., Sun, Z., Chen, S., 2020b. Reduction of structural impacts and distinction of photosynthetic pathways in a global estimation of GPP from space-borne solar-induced chlorophyll fluorescence. Remote Sensing of Environment 240, 111722.

Zhang, Z., Zhang, Y., Zhang, Q., Chen, J.M., Porcar-Castell, A., Guanter, L., Wu, Y., Zhang, X., Wang, H., Ding, D., 2020c. Assessing bi-directional effects on the diurnal cycle of measured solar-induced chlorophyll fluorescence in crop canopies. Agricultural Forest Meteorology 295, 108147.

Zhang, Z., Zhang, Y., Zhang, Y., Gobron, N., Frankenberg, C., Wang, S., Li, Z., 2020d. The potential of satellite FPAR product for GPP estimation: An indirect evaluation using solar-induced chlorophyll fluorescence. Remote Sensing of Environment 240, 111686.

Zhao, F., Dai, X., Verhoef, W., Guo, Y., van der Tol, C., Li, Y., Huang, Y., 2016. FluorWPS: A Monte Carlo ray-tracing model to compute sun-induced chlorophyll fluorescence of three-dimensional canopy. Remote sensing of environment 187, 385-399.